



1 Droplet collection efficiencies estimated from satellite retrievals 2 constrain effective radiative forcing of aerosol-cloud interactions

3 Charlotte M. Beall¹, Po-Lun Ma¹, Matthew W. Christensen¹, Johannes Mülmenstädt¹, Adam
4 Varble¹, Kentaroh Suzuki², Takuro Michibata³

5 ¹Atmospheric Sciences and Global Change Division, Pacific Northwest National Laboratory, Richland, WA, 99354,
6 U.S.A.

7 ²Atmosphere and Ocean Research Institute, University of Tokyo, Chiba, 277-8568, Japan

8 ³Department of Earth Science, Okayama University, Okayama, 700-8530, Japan

9 *Correspondence to:* Charlotte M. Beall; charlotte.beall@pnnl.gov

10

11 **Abstract.** Process-oriented observational constraints for the anthropogenic effective radiative forcing due to aerosol-
12 cloud-interactions (ERF_{aci}) are highly desirable because the large uncertainty associated with ERF_{aci} poses a
13 significant challenge to climate prediction. The satellite-based Contoured Frequency by Optical Depth Diagrams
14 (CFODD) analysis was previously proposed to support evaluation of model representation of cloud liquid to rain
15 conversion processes because the slope of a CFODD, generated from joint MODerate Resolution Imaging
16 Spectroradiometer (MODIS)-CloudSat cloud retrievals, provides an estimate of cloud droplet collection efficiency in
17 single-layer warm liquid clouds (SLWCs). Here we present an updated CFODD analysis as an observational constraint
18 for the ERF_{aci} due to warm rain processes and apply it to the U.S. Department of Energy's Energy Exascale Earth
19 System Model version 2 (E3SMv2). Updates to the CFODD analysis include multiple changes to the SLWC detection
20 algorithm for better consistency between MODIS-CloudSat observations and the satellite simulators, as well as the
21 estimation of CFODD slopes using Random Sample Consensus robust linear regression. A series of sensitivity
22 experiments shows that E3SMv2 droplet collection efficiencies and ERF_{aci} are highly sensitive to the treatment of
23 autoconversion, the rate of mass transfer from cloud liquid to rain, yielding a strong correlation between the CFODD
24 slope and the shortwave component of ERF_{aci} (Pearson's $R = -0.91$). We estimate the shortwave component of ERF_{aci}
25 (ERF_{aci,sw}), constrained by MODIS-CloudSat, by calculating the intercept of the linear association between E3SMv2
26 ERF_{aci,sw} and the CFODD slopes, using the MODIS-CloudSat CFODD slope as a reference. When E3SMv2's droplet
27 collection efficiency is constrained to agree with the A-Train retrievals, ERF_{aci,sw} is reduced by 13% in magnitude,
28 indicating that correcting bias in the ERF_{aci,sw} due to autoconversion would bring E3SMv2's total ERF_{aci} (-1.50 W m^{-2})
29 into better agreement with the IPCC AR6 'very likely' range for ERF_{aci} ($-1.0 \pm 0.7 \text{ W m}^{-2}$). This study provides
30 a new process-oriented observational constraint for ERF_{aci} due to warm rain processes to reduce the uncertainty of
31 climate predictions.

32



33 **1 Introduction**

34 Single-layer, low-level marine warm clouds cover 25% of the ocean surface (Charlson et al., 1987) and exert a strong
35 cooling effect on climate due to their reflectivity (Hartmann et al., 1992; Hartmann and Short, 1980; Ramanathan et
36 al., 1989). Aerosols modulate multiple radiative properties of low warm clouds, including droplet number
37 concentration (N_d), liquid water path (LWP), geometric thickness, cloud fraction, and lifetime, and their net impact
38 on the cloud radiative forcing is the most uncertain component of the climate system (e.g., Stevens and Feingold,
39 2009; Christensen et al., 2020; Glassmeier et al., 2021). Though aerosols also exert a significant influence on ice and
40 mixed-phase clouds, aerosol-cloud interactions (ACI) make their largest contribution to global radiative forcing via
41 liquid water clouds (Bellouin et al., 2020).

42 In marine warm cloud regimes, an increase in aerosol concentrations typically leads to increasing N_d . Given constant
43 condensed water content, enhanced aerosol concentrations increase cloud albedo due to higher concentrations of
44 smaller cloud droplets through the so-called “Twomey effect” (Twomey, 1974). However, the cooling effect of
45 increased N_d can be offset or enhanced by competing aerosol-mediated cloud properties such as cloud fraction and
46 LWP. For example, increased numbers of smaller droplets can diminish cloud fraction by reducing cloud droplet
47 sedimentation (Bretherton et al., 2007) and increasing cloud-top evaporation and dry air entrainment (Wang et al.,
48 2003). On the other hand, aerosols can also increase cloud fraction and vertical extent by suppressing precipitation
49 (Albrecht, 1989; Pincus and Baker, 1994). Christensen et al. (2020) demonstrated that the impact of aerosol on low-
50 level cloud areal coverage depends on the stability of the atmosphere: in thermodynamically stable lower tropospheric
51 conditions, increased aerosol results in increased cloud fraction, lifetime and N_d , whereas in unstable conditions,
52 entrainment and evaporation offset Twomey effects, resulting in relatively smaller changes to cloud radiative
53 properties.

54 Earth Systems Models (ESMs) are relied upon for estimating the global Effective Radiative Forcing of Aerosol-Cloud
55 Interactions (ERF_{aci}) due to the dearth of observations from the pre-industrial era. Yet ESM estimates are challenged
56 by the lack of observational constraints on ERF_{aci} and the cloud processes that modulate ERF_{aci}, which must be
57 parameterized due to the computational expense of explicitly resolving them. Mülmenstädt et al. (2020) proposed a
58 renewed focus on process-oriented observational constraints as a solution to “equifinality”, whereby differing
59 representations of cloud processes can reproduce observed state variables such as LWP and cloud fraction. The



60 problem of equifinality renders many global long-term observations of state variables useless for constraining ERFaci
61 on their own. Mülmenstädt et al. (2020) argues that constraints based on cloud process observations are thus highly
62 desirable as an alternative approach to state variable-based constraints because mitigating bias in a cloud process
63 representation will improve estimates of the response of the process to aerosols. Recent examples of process-based
64 diagnostics include the Earth System Model Aerosol-Cloud Diagnostics Package (ESMAC Diags) (Tang et al., 2022;
65 Tang et al., 2023), which supports evaluation of aerosol activation processes, and Varble et al. (2023) which
66 demonstrated multiple model-observations comparison approaches that target processes affecting cloud albedo
67 susceptibility using geostationary satellite data and surface-based observations. Christensen et al. (2023) applied
68 ground-based measurements, satellite retrievals and meteorological reanalysis products in a Lagrangian framework to
69 evaluate multiple aerosol-cloud processes in E3SM, including cloud condensation nuclei deposition via precipitation
70 and the temporal response in N_d to aerosol perturbations.

71 In response to the demand for process-oriented constraints on warm liquid cloud processes, we present a constraint on
72 the ERFaci due to autoconversion, a parameterization representing the transfer of liquid mass and number from the
73 cloud to rain category, based on satellite cloud retrievals. For the past 12 years, prior studies have applied the
74 Contoured Frequency by Optical Depth Diagrams (CFODD) analysis (Nakajima et al. 2010; Suzuki et al. 2010) to
75 evaluate model representation of warm rain processes because the slopes of CFODDs, generated from spaceborne
76 radar reflectivity profiles (CloudSat) (e.g. Marchand et al., 2008) and cloud property retrievals from the Moderate
77 Resolution Imaging Spectroradiometer (MODIS) (e.g. Platnick et al., 2017), provide an estimate of cloud droplet
78 collection efficiency in warm liquid clouds (Suzuki et al. 2010). To demonstrate how CFODD analysis can be applied
79 to constrain ERFaci due to autoconversion, we apply an updated CFODD analysis to MODIS-CloudSat retrievals
80 between June 2006 and April 2011 as well as the U.S. Department of Energy's Energy Exascale Earth System Model
81 version 2 (E3SMv2) in a series of autoconversion sensitivity experiments. We show that the shortwave component of
82 ERFaci (ERFaci_{sw}) can be constrained using the correlation between ERFaci_{sw} and CFODD slopes (i.e., the slope
83 computed from the in-cloud optical depth and CloudSat radar reflectivity, see Fig. 7 of Suzuki et al. 2010) using the
84 MODIS-CloudSat CFODD slope as a reference.

85 To support the application of CFODD analysis as a constraint on ERFaci_{sw}, we modified the Warm Rain Diagnostics
86 (WRDs) subroutine (Michibata et al. 2019) that was recently implemented in the Cloud Feedback Model



87 Intercomparison Project (CFMIP) Observations Simulator Package (COSPV2.0), a software package that supports
88 climate model evaluation against satellite observations (Michibata et al., 2019; Swales et al., 2018). The WRDs
89 support evaluation of model warm rain processes in single-layer warm liquid clouds (SLWCs) based on joint statistics
90 from MODIS and CloudSat. The first diagnostic provides the fractional occurrence of SLWCs, classified as non-
91 precipitating, drizzling, or raining clouds based on CloudSat column maximum radar reflectivity. The second
92 diagnostic is the CFODD, which is the probability density function (PDF) of radar reflectivity as a function of in-
93 cloud optical depth (ICOD), where ICOD is the optical depth integrated from the cloud top downward to each vertical
94 layer and represents an in-cloud vertical coordinate (Nakajima et al., 2010; Suzuki et al., 2010). The CFODD shows
95 how vertical cloud microphysical structures transition from non-precipitating to precipitating as a function of cloud-
96 top effective radius (R_e), and the slope of reflectivity change with ICOD provides an estimate of droplet collection
97 efficiency factor (Suzuki et al., 2010). Previous studies have used CFODDs to demonstrate that pollution decreases
98 droplet collection efficiency, suppressing rainfall near the cloud base (Mangla et al., 2020; Michibata et al., 2014;
99 Suzuki et al., 2013), and to evaluate model cloud liquid to rain conversion processes against satellite observations
100 (Suzuki et al., 2015; Jing et al. 2019; Michibata and Suzuki, 2020). Modifications to the WRDs include additional
101 diagnostics that provide SLWC sampling statistics to illuminate how sample size affects CFODD results, the
102 implementation of a CloudSat ground-clutter mask in the simulated WRDs and updates to SLWC selection criteria
103 for better consistency between observations and satellite simulators.

104 **2 Warm Rain Diagnostics Overview**

105 The WRDs and their implementation in COSPV2.0 were described in Michibata et al. (2019). The WRDs are designed
106 to run online with the host model, accumulating time step statistics on warm rain cloud processes for subcolumns to
107 mitigate the risk of data-processing bottlenecks associated with outputting large data volumes. COSPV2.0 generates
108 ensembles of stochastic subcolumns from model gridbox-mean variables to emulate model subgrid variability and to
109 resolve discrepancies in spatial resolution between observations and the model grid (Swales et al., 2018).

110 To generate observational reference data for model evaluation, Michibata et al. (2019) used the MODIS and CloudSat
111 products 2B-TAU R04 (Polonsky, 2008) and 2B-GEOPROF R04 (Mace et al., 2007; Marchand et al., 2008),
112 respectively, for SLWC detection between June 2006 and April 2011. The criteria for SLWC detection are described
113 in Supplement Table S1. Model-simulated SLWCs are detected using COSPV2.0 simulated CloudSat reflectivity and



114 multiple MODIS cloud properties, including ice water path (IWP), liquid water path (LWP), cloud-top effective radius
115 (R_e), and cloud optical thickness (COT) (Table S1). For the SLWC fractional occurrence (frequency) diagnostic,
116 SLWCs are binned by precipitation intensity according to the maximum column CloudSat reflectivity (Z_{max}), where
117 non-precipitating, drizzling and raining SLWCs correspond to $Z_{max} < -15 \text{ dBZ}_e$, $-15 \text{ dBZ}_e \leq Z_{max} < 0 \text{ dBZ}_e$,
118 and $Z_{max} \geq 0 \text{ dBZ}_e$, respectively. The SLWC fractional occurrence diagnostic features frequency of each
119 precipitation type relative to the total SLWC population.

120 To support evaluation of liquid cloud collection efficiencies and cloud to rain transition processes, CFODDs are
121 constructed from the PDFs of CloudSat reflectivity profiles binned by ICOD. ICOD is parameterized as a function of
122 MODIS COT by invoking the adiabatic condensation growth model to vertically slice the column COT into each layer
123 (Suzuki et al., 2010). The slope of the resulting 2D-PDF diagnostic yields an estimate of droplet collection efficiency,
124 with steeper slope implying higher efficiency.

125 In this study, CFODD slopes are estimated using RANdom SAMple Consensus (RANSAC) robust linear regression.
126 RANSAC was chosen for performing linear regression due to the right-skewed distribution of CFODD datasets. The
127 regression is applied to the CFODD distribution at $4 \leq \text{ICOD} \leq 20$ and $Z < 20 \text{ dBZ}$ to reduce the effect of the Mie
128 scattering regime where the radar reflectivity can be saturated and to restrict analysis to profiles where the uncertainty
129 of MODIS COT retrievals is lower as error can be higher in optically thin liquid clouds (e.g., $\text{COT} < 4$) (Platnick et
130 al., 2017). The uncertainty in the RANSAC slope calculation is estimated by “bootstrapping”, repeatedly performing
131 RANSAC regressions on 1000 random subsamples of 80% the CFODD dataset to generate a distribution of slope
132 estimates. The 1-sigma error and 98% confidence intervals were calculated from this distribution. The residual
133 threshold applied for RANSAC outlier detection was 0.1 and 0.5 x median absolute error (MAE) for MODIS-CloudSat
134 and E3SMv2, respectively. Data points with MAE exceeding the residual threshold are excluded from the linear
135 regression in RANSAC.

136 **2.1 E3SMv2**

137 Several updates to the WRDs are described in Sect. 2.2, the impacts of which are demonstrated through an application
138 of the updated WRDs to the U.S. Department of Energy’s Energy Exascale Earth System Model v2 (E3SMv2). The
139 atmosphere component of the model, E3SM Atmosphere Model v2 (EAMv2), is described in detail in Golaz et al.
140 (2022). Like its predecessor EAMv1, EAMv2 predicts stratiform and shallow cumulus cloud macrophysics through



141 the Cloud Layers Unified by Binormals (CLUBB) parameterization, which unifies the treatment of planetary boundary
142 layer turbulence, shallow convection, and cloud macrophysics through a higher-order turbulence closure scheme
143 (Bogenschutz et al., 2013; J. C. Golaz et al., 2002; Larson, 2017; Larson & Golaz, 2005). CLUBB diagnoses cloud
144 fraction and cloud liquid water from a joint double-Gaussian PDF. Ice and liquid cloud fractions in CLUBB are
145 analytically diagnosed by integrating saturated proportions of the joint PDF (Guo et al. 2015).

146 Cloud microphysics is represented with the “Morrison and Gettelman version 2” (MG2) scheme (Gettelman and
147 Morrison, 2015). MG2 prognoses the mass mixing ratios and number concentrations of cloud liquid, ice and
148 precipitation hydrometeors. The coupled MG2 cloud microphysics and CLUBB higher-order turbulence
149 parametrization explicitly provides values for hydrometer mass and number mixing ratios as well as cloud fraction.
150 Deep convection is represented by the Zhang and McFarlane (1995) (ZM) scheme. As convective cloud fraction is
151 not parameterized in the mass-flux based ZM scheme, it is diagnosed from the cloud mass flux for cloud radiation
152 calculation (Hack et al., 1993). The total cloud fraction in EAMv2 combines CLUBB, deep convective cloud fractions
153 and ice cloud fraction following (Park et al., 2014). The four-mode version of the Modal Aerosol Module (MAM4) is
154 used to predict aerosol properties and processes (Liu et al., 2012, 2016; H. Wang et al., 2020).

155 EAMv2 runs on 72 vertical atmospheric levels with a top at 0.1h Pa (Rasch et al., 2019; Xie et al., 2018). However,
156 distinct from its predecessor EAMv1, EAMv2 has two separate parameterized physics and dynamics grids (Hannah
157 et al., 2021), with average horizontal grid spacings of ~165 km and ~110 km, respectively.

158 A six-year E3SMv2 simulation with transient, present-day forcing was run between 2006 and 2011 with online
159 COSPv2.0 for comparison with A-Train observations of SLWCs, allowing one additional year (2005) for model spin-
160 up. To facilitate comparison with observations, large-scale winds were constrained via the “nudging” technique (Lin
161 et al., 2016; Ma et al., 2014; Zhang et al., 2014), in which horizontal and vertical winds are relaxed toward the Modern
162 Era-Retrospective Analysis for Research and Applications, Version 2 (MERRA2) reanalysis data (Gelaro et al., 2017)
163 with a 6-hour time-scale. MERRA2 data are read in every 3 hours and linearly interpolated to model times. COSPv2.0
164 is called at every time step (0.5 h) and run with 10 subcolumns. We observed little change in CFODD results for
165 increased numbers of subcolumns of 20 to 50.

166 **2.2 COSPv2.0**



167 Cloud-observing instrument simulators support evaluation of model cloud representation by translating gridbox-mean
168 model variables (e.g., cloud fraction, hydrometeor mass mixing ratio, precipitation) into quantities that are measured
169 by a cloud sensor (e.g., reflectivity). COSPv2.0 includes multiple cloud-observing satellite simulators and has been
170 used extensively to diagnose issues in model cloud representation (Cesana & Chepfer, 2012; Kay et al., 2016; Song
171 et al., 2018a; Y. Zhang et al., 2010). Recently, M. Zhang et al. (2022) used the COSPv2.0 CALIPSO simulator to
172 demonstrate that changes to the Wegener-Bergeron-Findeisen process in EAMv2 decreased an ice cloud fraction low
173 bias in the Arctic compared to EAMv1 but did not correct excesses of supercooled liquid.

174 There are known limitations to COSPv2.0 that affect its application to E3SM for cloud representation evaluation. The
175 subgrid distribution of cloud variables generated by COSPv2.0 does not match E3SM subgrid variability.
176 Hydrometeor species are distributed homogeneously across the subcolumns generated by COSPv2.0 via the
177 subcolumn generator SCOPS (Subcolumn Cloud Overlap Profile Sampler) (Klein and Jakob, 1999), such that the
178 ensemble of subcolumns reproduces the gridbox cloud fraction but not the subgrid distribution of liquid and ice within
179 the simulated clouds (Dewald, 2021). Song et al., (2018b) demonstrated that the default “homogeneous hydrometeor
180 scheme” from SCOPS results in overestimation of radar reflectivity in warm liquid clouds, thus overestimating
181 precipitating clouds since maximum column reflectivity is often used to distinguish precipitating clouds (as in the
182 WRDs). Errors in simulated satellite retrievals have also been attributed to SCOPS overlap assumptions (Hillman et
183 al., 2018). Such a bias from SCOPS can result in unfair observational evaluation of a host model such as E3SMv2.
184 Inconsistencies in microphysical assumptions between the host model and COSP pose another challenge. While many
185 microphysical assumptions in COSPv2.0 can be configured for agreement with E3SMv2 microphysics (MG2), some
186 inconsistencies remain, including gamma distribution shape parameters for hydrometeor size distributions and
187 hydrometeor vertical overlap assumptions (J. Wang et al., 2021). Next-generation E3SM development includes efforts
188 to improve agreement in the subgrid variability and microphysical assumptions involved in forward simulating
189 satellite retrievals. Other issues include the simplified treatment of satellite cloud detection in simulators. For example,
190 the CloudSat Cloud Profiling Radar (CPR) cloud mask value threshold ≥ 30 is applied for cloud detection in the
191 WRDs’ A-Train analysis to indicate “good” or “strong” echo with high confidence detection (see next section and
192 Supplement Table 1). The CPR cloud mask confidence levels consider signal-to-noise ratios, horizontal averaging,
193 and spatial continuity (Marchand et al., 2008), but as this cloud mask is not available in COSPv2.0, CloudSat cloud
194 detection is simulated by applying a reflectivity threshold $-30 \leq Z_e \leq 20$ dBZ.



195 The WRDs rely on COSPv2.0 simulated MODIS and CloudSat retrievals. The WRDs in COSPv2.0 work as follows:
196 First, COSPv2.0 takes in model atmospheric state and cloud variables including temperature, pressure, water vapor
197 and hydrometeor mass mixing ratios, hydrometeor R_e , large-scale stratiform cloud fraction, convective cloud fraction
198 and precipitation rate. The COSPv2.0 subcolumn generator SCOPS then produces subgrid distributions of clouds and
199 precipitation for better comparison with smaller scale satellite pixel measurements. SCOPS subcolumns are
200 homogenous, discrete samples generated such that a sufficiently large ensemble reproduces the model column profile
201 of bulk cloud properties (Webb et al., 2001; Swales et al., 2018). SCOPS assigns each subcolumn a type (large-scale
202 stratiform, convective or clear-sky) according to the host model's convective and large-scale stratiform cloud fraction.
203 Cloud properties such as hydrometeor mass mixing ratios and R_e are distributed homogeneously across the
204 subcolumns by cloud type (i.e., all stratiform cloud subcolumns are assigned the same stratiform ice and liquid mixing
205 ratios as SCOPS only takes total convective and stratiform cloud fraction as input, and does not consider stratiform
206 liquid and ice cloud fraction in its default configuration. "Maximum-random" cloud overlap is applied to subcolumns,
207 consistent with the model parameterizations). The MODIS and CloudSat simulators apply simplified versions of their
208 respective retrieval algorithms to each subcolumn, emulating MODIS retrievals of cloud properties, radar reflectivity
209 and lidar backscatter, respectively. Gridbox-mean values are estimated from accumulated subcolumn statistics. The
210 WRDs take as inputs gridbox-mean simulated MODIS retrievals of LWP, IWP, COT and R_e , as well as subcolumn
211 CloudSat reflectivity profiles. Deviations from the original WRDs implemented in COSPv2.0 (Michibata et al., 2019b)
212 include the application of the simulated CloudSat ground-clutter filter (available in COSPv2.0, but not applied to the
213 WRDs previously) for better comparison with CloudSat retrievals, and the elimination of the "fracout" input used in
214 the SLWC detection scheme from SCOPS. "Fracout" is the subcolumn-level cloud classification by vertical level from
215 SCOPS, where each level of each subcolumn is designated as large-scale stratiform, convective, or clear-sky. This
216 input was removed from the WRDs' SLWC detection algorithm because of the lack of comparable cloud-type
217 designation in the observations and CloudSat simulator and because "fracout" vertical cloud profiles were observed
218 to deviate significantly from CloudSat reflectivity profiles (i.e., fracout indicates clear-sky where CloudSat reflectivity
219 indicates cloud, or vice versa).

220 **2.3 Satellite data**



221 The MOD06-1KM-AUX R05 product (Platnick et al., 2017), which provides MODIS collection 6 retrievals along the
222 CloudSat footprint, supplied the 6 MODIS cloud retrievals required for the SLWC detection described in Suzuki et
223 al. (2010): LWP, IWP, R_c , COT, cloud top pressure and cloud layer number. Atmospheric temperature profiles were
224 obtained from ECMWF-AUX R05, which includes temperature profiles from the European Centre for Medium-Range
225 Weather Forecast (ECMWF) interpolated to the CloudSat footprint. 2B-GEOPROF R05 provided the CloudSat
226 reflectivity profiles, the Cloud Profiling Radar (CPR) cloud mask and echo top characterization (Marchand et al.,
227 2008). The detection of SLWCs and CFODD analysis in the present study follows Suzuki et al. (2010) (see
228 Supplement Table 1 for details) with one exception: a COT threshold was decreased from 15 to 0.3; this had a
229 substantial impact on cloud occurrence (Figure 1; described next) and is consistent with the COT threshold
230 implemented in the COSPv2.0 WRDs.

231 **2.4 Autoconversion sensitivity experiments and ERFaci**

232 The autoconversion parameterization in E3SMv2 is a modified Khairoutdinov & Kogan (2000) scheme (hereafter,
233 KK2000), in which coefficients were updated in response to large uncertainties in different cloud regimes and to
234 improve fidelity in climate simulations. The KK2000 autoconversion scheme is $\frac{\delta q_r}{\delta t_{auto}} = A Q_c^\alpha N_d^\beta$, where q_r is
235 the rainwater mixing ratio, Q_c is the cloud water mixing ratio, N_d is the cloud droplet number concentration, and A , α
236 and β are the modified coefficients.

237 To develop a constraint on the ERFaci due to autoconversion, we performed multiple pairs of simulations featuring
238 preindustrial (PI) and present-day (PD) aerosol emissions. In each pair of simulations, one of the three coefficients
239 (A , α or β) was modified to its KK2000 value, a value reported by Wood (2005) or a value within a range bounded by
240 the three studies. One additional experiment on the KK2000 parameterization for the accretion rate was performed,
241 the formulation of which is $\frac{\delta q_r}{\delta t_{accre}} = F_1 F_2 67 (Q_c Q_r)^{1.15} \rho^{-1.3}$, where Q_r is the rain water mixing ratio, F_1 represents
242 subgrid Q_c variability, ρ is air density, and F_2 is an accretion rate enhancement factor. F_2 was increased by a factor of
243 ~ 3 in the accretion sensitivity experiment. F_2 is considered a tunable parameter in E3SM (Ma et al., 2022). The
244 experiment details are provided in Table 1.



245 Table 1. KK2000 coefficient and accretion enhancement factor values applied in 12 sensitivity experiments. Dash (“-”
 246 “”) indicates the coefficient value was unchanged from the default E3SMv2 parameterization (equal to the “CNTL”
 247 simulation value).

Name	A	α	β	accre
CNTL	3.05E4	3.19	-1.4	1.75
alpha01	-	4.22	-	-
beta01	-	-	-1.0	-
acoe01	3.05E6	-	-	-
alpha02	-	2.47	-	-
acoe02	1.35E3	-	-	-
alpha03	-	3.00	-	-
beta03	-	-	-1.79	-
beta04	-	-	-3.01	-
acoe05	3.05E5	-	-	-
acoe06	1.53E5	-	-	-
acoe07	1.53E6	-	-	-
accre01	-	-	-	5

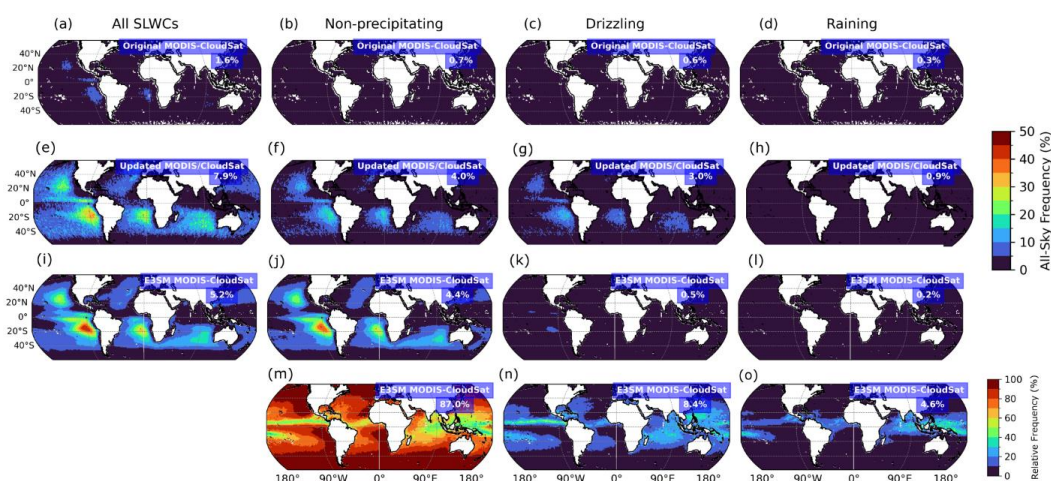
248

249 ERF_{aci} for each pair of simulations was calculated following the Ghan (2013) method, where $ERF_{aci} = \Delta(F_{clean} -$
 250 $F_{clear, clean})$. F_{clean} is the radiative flux at the top-of-atmosphere (TOA) neglecting the absorption and scattering of
 251 aerosols, and $F_{clear, clean}$ is the radiative flux at the TOA neglecting both clouds and the absorption and scattering of
 252 aerosols. The Δ indicates the PD – PI difference. While the PD-PI approach is a common strategy for estimating
 253 ERF_{aci}, Christensen et al. (2023) demonstrated that it may yield a different estimate than the PD approach, where
 254 components of ERF_{aci} (LWP adjustment, N_d adjustment, cloud fraction adjustment) are estimated by regressions of
 255 cloud properties multiplied by the anthropogenic aerosol fraction. We calculate ERF_{aci} for SLWCs only, binned by
 256 the MODIS R_c range corresponding to the CFODD analysis.

257 3 Updates to MODIS and CloudSat SLWC analysis and reference data



258 The first diagnostic in the original WRDs featured relative frequencies of SLWCs by precipitation intensity in both
 259 the A-Train reference data and the COSPv2.0 output (e.g., Fig. 1 m-o). We have updated this diagnostic with all-sky
 260 frequencies and by decreasing the lower MODIS COT threshold from 15 to 0.3, for consistency with the WRDs
 261 implemented in COSPv2.0 (Fig. 1 a-l). SLWCs featured in Fig. 1 and all following figures and analyses are ocean-
 262 only due to higher uncertainties in MODIS retrievals over land (Platnick et al., 2017).



263

264 **Figure 1.** All-sky frequencies of total SLWCs June 2006 – Apr 2011, non-precipitating ($Z_{max} < -15 \text{ dBZ}_e$), drizzling
 265 ($-15 \text{ dBZ}_e \leq Z_{max} < 0 \text{ dBZ}_e$) and raining ($Z_{max} \geq 0 \text{ dBZ}_e$) ocean-only SLWCs according to original reference analysis of
 266 MODIS and CloudSat observations (Michibata et al., 2019a, 2019b) Michibata et al., 2019a, 2019b) Michibata et al., 2019a, 2019b)
 267 (a-d), updated reference MODIS and CloudSat analysis (e-h) and E3SMv2-COSPv2.0 (i-l). Figures m-o show frequencies of non-
 268 precipitating, drizzling and raining SLWCs relative to the total SLWCs simulated by E3SMv2. Values in blue boxes indicate global
 269 ocean-only grid-weighted mean frequency. SLWCs were undersampled in original reference A-Train analysis by a factor of ~5.
 270 Compared to the original reference A-Train data, the updated analysis demonstrates that E3SM underrepresents rather than
 271 overrepresents total SLWC frequency and that precipitating SLWCs are underrepresented by a factor of 6 compared to observations.
 272 Figure 1 also shows that decreasing the lower MODIS COT threshold from 15 to 0.3 in the updated A-Train analysis
 273 (Sect. 2.3) increased total SLWC sampling by 5-fold (global ocean mean, see Sect. 2.3) compared to the original
 274 CFODD analysis in Michibata et al. (2019a) and Michibata et al. (2019b). The increase in SLWC sampling in the
 275 reference data affects multiple outcomes of the model evaluation in this case: E3SMv2 underrepresents, rather than
 276 overrepresents, total SLWCs, and the SLWCs that are missing from E3SMv2 are entirely the precipitating SLWC

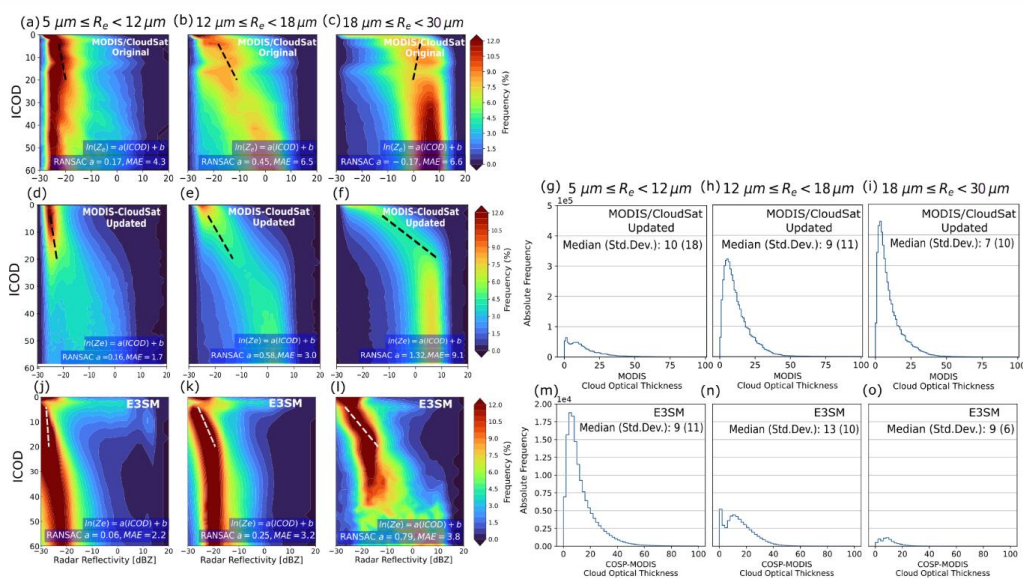


277 populations. The underrepresentation of precipitating SLWCs in E3SMv2-COSP indicates that any bias from SCOPS
278 towards increased precipitation in warm liquid clouds is relatively minor (Sect. 2.2; Song et al. (2018)). Not all the
279 differences between the original and updated reference data can be explained by the change in COT threshold,
280 however, as we were unable to reproduce the original CFODD data with the updated satellite products used in this
281 study. Fig. S1 and S2 show that increasing the lower COT threshold from 0.3 to 15 yields SLWC frequencies that are
282 much closer to the original reference data (+25%) than the updated reference data, but significant differences remain
283 in the CFODDs.

284 The effects of the increased SLWC sampling in the A-Train reference data also significantly affected the CFODDs
285 and thus the comparison between A-Train and E3SMv2 droplet collection efficiencies. Figure 2 shows CloudSat
286 reflectivity frequency binned by ICOD for the original A-Train reference data (Fig. 2 a-c), the updated A-Train
287 reference data (d-f) and E3SMv2 (j-l), and RANSAC robust linear regression slopes at $4 \leq \text{ICOD} \leq 20$. In comparisons
288 with various other linear regression techniques, we found that RANSAC best supported the comparison of CFODD
289 slopes between E3SMv2 and observations because of the right-skewed distribution of CloudSat reflectivities at $0 \leq$
290 $\text{ICOD} \leq 20$ in E3SMv2 CFODDs (Figs. 2 j-l). RANSAC minimizes the median absolute error (MAE) and is less
291 sensitive to strong outliers in the dimension of the predicted variable (Z_e in this case) compared to other linear
292 regression techniques.

293 The updated A-Train CFODD distributions are significantly different than the original CFODD distributions (2D-
294 Kolmogorov-Smirnov test, $p \ll 0.05$). Compared to updated A-Train CFODDs, the E3SMv2 CFODDs show
295 decreased droplet collection efficiencies and an increased range of reflectivities near the cloud top in all size bins,
296 indicating that regardless of R_e , SLWCs are drizzling and raining near the cloud top with significantly higher frequency
297 than SLWCs in observations but have decreased collection efficiency below cloud top compared to MODIS-CloudSat.

298



299

300 **Figure 2.** Contoured frequency by optical depth diagrams (CFODDs) for SLWCs June 2006 – April 2011 binned by MODIS cloud
 301 top effective radius (R_e) from original reference MODIS-CloudSat observations analysis (a-c), updated reference MODIS-CloudSat
 302 observations analysis (d-f), and E3SMv2 (j-l). Random Sample Consensus (RANSAC) linear regressions were applied to the
 303 CFODD at $4 \leq \text{ICOD} \leq 20$ to estimate droplet collection efficiencies. RANSAC slopes and Median Absolute Error (MAE) values
 304 are shown in blue boxes. Droplet collection efficiencies increase with MODIS R_e as expected, except for the largest R_e size bin in
 305 the original reference data (Fig. 2c). Figs. g-i and m-o show absolute frequencies of SLWCs by MODIS COT, demonstrating that
 306 E3SMv2 overrepresents SLWCs with small R_e relative to medium and large R_e , compared to observations.

307 The high reflectivities near the cloud top are pronounced in the subset of E3SMv2 SLWCs with $4 < \text{MODIS COT} <$
 308 20 (Fig. S3), indicating that the high reflectivity at low ICOD in Figs. 2 (j-l) are not just a product of a subset of highly
 309 reflective, optically thin SLWCs, but that high reflectivities near cloud top within optically thicker SLWCs also
 310 contribute to this strange feature in the CFODD. The reflectivity profiles used to generate the CFODD come from the
 311 CloudSat simulator, which was not modified for this study. Examples of simulated CloudSat reflectivity profiles in
 312 SLWCs with $Z_e > 0$ dBZ near cloud top are shown in Fig. S4. The source of this issue and its implications for
 313 E3SMv2 representation of liquid cloud properties warrant further investigation that is beyond the scope of the present
 314 study.



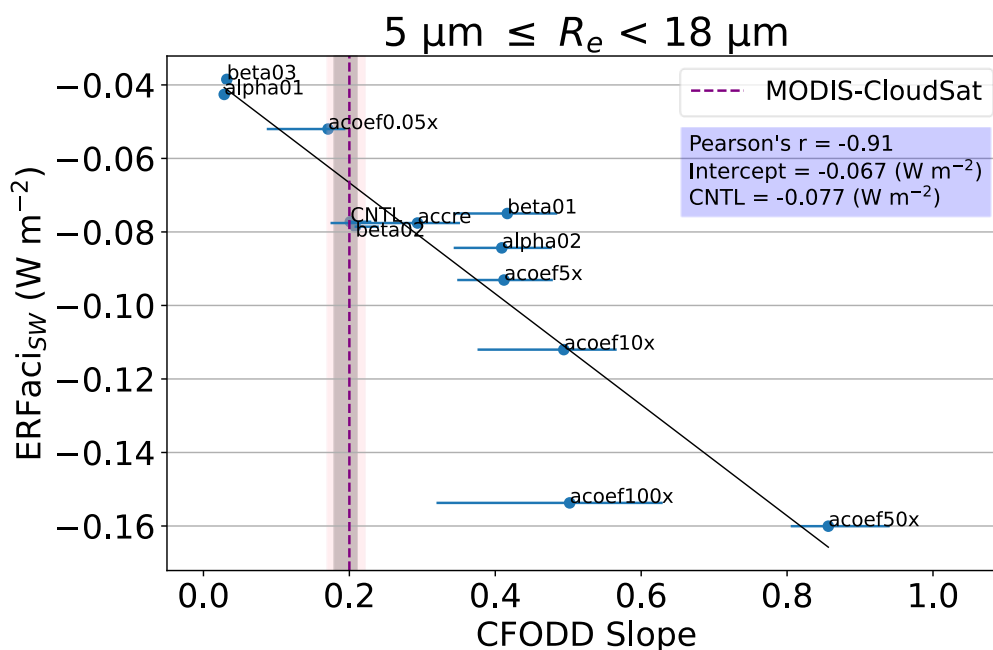
315 Absolute frequencies of SLWCs binned by MODIS COT for each CFODD R_e bin are shown for the updated A-Train
316 analysis (Fig. 2 g-i) and E3SMv2 only (Fig. 2 m-o). Note, this information was unavailable in the original reference
317 data (Michibata et al., 2019a). Compared to COT distributions in the updated A-Train analysis, E3SMv2 shows
318 decreasing SLWC frequency with R_e and an underrepresentation of SLWCs with large R_e , which aligns with the
319 underrepresentation of precipitating SLWCs in Fig. 1. Fig. 2o also shows that few SLWCs with large R_e have a COT
320 > 20 , indicating that the CFODD reflectivity profile in Fig. 2l at ICOD > 20 is comprised of few samples. The SLWC
321 COT PDFs have been implemented in the WRDs to support the interpretation of CFODD statistics.

322 **4 CFODD analysis to constrain ERF_{aci}**

323 To demonstrate the potential of the CFODD analysis described above for constraining ERF_{aci,sw} due to warm rain
324 processes, we performed 12 experiments featuring variations of E3SMv2's autoconversion and accretion
325 parameterizations and computed ERF_{aci,sw} following Ghan (2013; see Sect. 2.4). In each experiment, a single
326 coefficient of either the KK2000 autoconversion or accretion parameterization was perturbed, each of which is treated
327 as a tunable parameter in E3SMv2. The uncertain KK2000 coefficients, coupled with parameterization simplifications
328 (e.g., bulk moments and assumed droplet size distributions), result in uncertainties and biases in the model
329 representation of raindrop formation and growth. The experiments are described in Table 1, and the CFODDs for each
330 experiment are shown in Fig. S5.

331 Figure 3 shows a strong negative correlation between E3SMv2 ERF_{aci,sw} and the combined “small” and “medium”
332 R_e CFODD slope ($5 \leq R_e < 18 \mu\text{m}$, Pearson's $R = -0.91$). SLWCs with large R_e ($18 \leq R_e < 30 \mu\text{m}$) were excluded from
333 the analysis in Fig. 3 because this population represents a negligible fraction of total SLWCs in E3SMv2 (see Fig.
334 S6), resulting in poor sampling statistics and larger regression uncertainties. The correlation between ERF_{aci,sw} and
335 CFODD slope is stronger in the combined CFODDs relative to the CFODDs considered separately (Fig. S7, also see
336 discussion below). As CFODD slopes represent an estimate of droplet collection efficiency, Fig. 3 indicates that
337 ERF_{aci,sw} strengthens (increases in magnitude) with increasing droplet collection efficiency in E3SMv2 SLWCs with
338 R_e between 5 and 18 μm .

339



340

341 **Figure 3.** Linear regression between E3SMv2 ERFaci_{sw} and CFODD slopes, generated from SLWCs with MODIS R_e between 5
 342 and 18 μm , in 12 PD autoconversion and accretion sensitivity experiments. Results show a strong negative correlation between
 343 E3SMv2 ERFaci_{sw} and CFODD slopes. We constrain the ERFaci_{sw} by predicting the ERFaci_{sw} value at the reference MODIS-
 344 CloudSat $5 \leq R_e < 18 \mu\text{m}$ CFODD slope (purple dashed line) from the linear regression (intercept shown in blue box). The
 345 constrained ERFaci_{sw} value is decreased by 13% in magnitude compared to the CNTL simulation. Error bars represent 1-sigma
 346 error estimated from RANSAC-fit bootstrapping (Sect. 2). Grey and pink shaded regions indicate the 68 and 98% confidence
 347 intervals for the MODIS-CloudSat CFODD slope, respectively. Labels indicate the sensitivity experiment names (Table 1).

348 We constrain ERFaci_{sw} due to autoconversion uncertainties using the linear regression in Fig. 3 and the MODIS-
 349 CloudSat CFODD slope (Fig. S8) as a reference. The ERFaci_{sw} predicted by the linear regression at the MODIS-
 350 CloudSat slope value is -0.067 W m^{-2} , a 13% decrease in magnitude compared to the ERFaci_{sw} value predicted by the
 351 E3SMv2 CNTL simulation (-0.077 W m^{-2}). E3SMv2's total ERFaci (-1.50 W m^{-2}) falls within the IPCC AR6 'very
 352 likely' range for ERFaci ($-1.0 \pm 0.7 \text{ W m}^{-2}$), but our results indicate that correcting for the bias in ERFaci_{sw} due to
 353 autoconversion uncertainties would decrease the magnitude of ERFaci_{sw} and bring the predicted total ERFaci closer
 354 to the median IPCC ERFaci value (Forster et al., 2021).



355 Base cloud processes that are independent of aerosol contribute significantly to ERF_{aci} estimates (Mülmenstädt et al.,
356 2020). Autoconversion perturbations affect base cloud state (e.g., LWP, cloud fraction) and could, for example, cause
357 stronger ERF_{aci} by increasing cloud amount rather than increasing the impact of ACI on SW radiative forcing. Jing
358 et al. (2019) evaluated different autoconversion parameterization schemes in an ESM using the CFODD analysis
359 described in Michibata et al. (2019b) and found that the autoconversion scheme that yielded the best warm rain
360 representation predicted a significantly stronger ERF_{aci} that exceeded the uncertainty range of the IPCC AR5 and
361 canceled out much of the warming trend of the last century. The conflict between process representation and ERF_{aci}
362 predictions in Jing et al. (2019) underscore a challenge with process-based constraints: improving the representation
363 of a process can result in adverse outcomes to climate prediction due to compensating biases in the model. This
364 challenge is particularly troublesome for constraints on processes like autoconversion that affect the base cloud state
365 because decreasing autoconversion rates can increase total cloud amount, which can yield stronger ERF_{aci}. Thus, a
366 decreased autoconversion rate may improve precipitation outcomes in an ESM that presents the common “too
367 frequent” warm rain bias (e.g., Stephens et al., 2010), yet cause improbably strong ERF_{aci}. Our results show, however,
368 that decreased autoconversion rates result in weaker ERF_{aci} (Fig. 3), demonstrating that the base cloud state issue
369 presented in prior studies of autoconversion is not a dominant factor contributing to the ERF_{aci} of warm rain processes
370 in E3SMv2.

371 Fig. S9 shows the linear relationship between ERF_{aci,SW} normalized by the PI SW Cloud Radiative Effect (SWCRE),
372 which represents the fraction of ERF_{aci} that is independent of base cloud state changes, and CFODD slope. The
373 correlation coefficient in Fig. S7 (Pearson’s R = 0.74) is decreased compared to Fig. 3 (Pearson’s R = 0.91). However,
374 comparing the negative correlations between CFODD slope and PI cloud fraction (Fig. S10; Pearson’s R = -0.64) and
375 LWP (Fig. S11; Pearson’s R = -0.89) with Fig. 3, the ERF_{aci,SW} increases in magnitude as LWP and cloud fraction
376 decrease, further demonstrating that the contribution of base cloud state to ERF_{aci,SW} is relatively minor. The decreased
377 correlation coefficient in Fig. S6 could also be influenced by poor sampling statistics in the “acoef100x” experiment.
378 The acoef100x was the only one of six experiments involving perturbations of the “A” coefficient in KK2000 (Table
379 1; Sect. 2.4) in which the CFODD slope did not increase with an increase in magnitude of the “A” coefficient. Given
380 the significant decrease in SLWC cloud fraction in this experiment compared to the others (Fig. S10, Table S2), the
381 CFODD slope result may be affected by insufficient sample size, an additional uncertainty of the CFODD linear
382 regression that is not reflected in the bootstrapping-based uncertainty estimate (Sect. 2). While we derive a constraint



383 for $ER_{Faci_{SW}}$ using the combined small and medium R_e CFODDs, when the R_e subsets are considered individually,
384 they show distinct contributions to $ER_{Faci_{SW}}$. Fig. S7 shows that SLWCs with small R_e have a negative $ER_{Faci_{SW}}$,
385 but that SLWCs in the medium and large R_e subsets have positive $ER_{Faci_{SW}}$ values. This indicates that the dominant
386 effect of aerosols on shortwave radiative forcing in the medium and large SLWC subsets is decreased cloud fraction,
387 which is reflected in the decreased SLWC sample sizes in the PD simulations compared to PI (Fig. S12, S13). The
388 negative linear relationship between $ER_{Faci_{SW}}$ and CFODD slope in the medium and large R_e subsets indicates that
389 increasing droplet collection efficiency partially counteracts the decrease in cloud fraction due to aerosol. The small
390 R_e SLWCs, however, show a negative correlation between $ER_{Faci_{SW}}$ and CFODD slope, indicating that the dominant
391 effect of aerosols on this subset via decreasing of the CFODD slope is to strengthen $ER_{Faci_{SW}}$. The combined small
392 and medium CFODD and $ER_{Faci_{SW}}$, therefore, represent the convolution of two populations with differing $ER_{Faci_{SW}}$
393 sensitivities to autoconversion perturbations. We chose to constrain $ER_{Faci_{SW}}$ using the combined small and medium
394 CFODD and $ER_{Faci_{SW}}$ due the correlation performance and the dearth of large R_e SLWCs in E3SMv2. However,
395 constraints for $ER_{Faci_{SW}}$ could potentially be derived for each individual R_e subset or various combinations thereof,
396 depending on the distribution of SLWCs among the R_e size bins and their contribution to the host model's ER_{Faci} .
397 Considering that constrained $ER_{Faci_{SW}}$ increases in magnitude with increasing R_e in Fig. S7 the underrepresentation
398 of SLWCs with large R_e in E3SMv2 represents a compensating bias, without which the total ER_{Faci} bias would be
399 even larger compared to IPCC AR6.

400 There are multiple limitations to the CFODD analysis that should be considered in its application as a constraint for
401 ER_{Faci} . First, droplet collection is not explicitly represented in ESMs with bulk microphysical schemes such as
402 E3SMv2, but is instead implicit in an amalgamation of process and drop size distribution parameterizations controlling
403 the evolution of the cloud and precipitation. Delving into the impact of these individual processes on CFODD-based
404 constraint of ER_{Faci} is a good target of future work, while autoconversion modulation of ER_{Faci} was the primary
405 focus here. Furthermore, simulated radar reflectivity is highly sensitive to particle size distribution assumptions in the
406 forward simulator (e.g., Bodas-Salcedo et al., 2011; J. Wang et al., 2021). The host model, therefore, could represent
407 warm rain microphysical processes with high fidelity but still produce biased CFODD profiles when compared with
408 observations. In COSPv2.0, the CloudSat simulator calculates size distributions from an assumed distribution (e.g.,
409 log-normal, gamma, exponential) as well as mass-mixing ratios, precipitation fluxes, and gridbox-mean R_e from the
410 host model. Default COSPv2.0 size distributions were used in this study: log-normal for large-scale stratiform and



411 convective cloud liquid, and exponential for large-scale stratiform and convective cloud rain. The CFODD analysis
412 itself is subject to multiple uncertainties, including the use of simple adiabatic and condensational growth assumptions
413 to scale MODIS COT to ICOD. These assumptions result in a vertical distribution of optical depth, mass
414 concentrations and particle size that may not reflect reality. For example, in the CFODD, particle size and mass
415 concentration are assumed to monotonically increase with height, yet in the real cloud, particle sizes may decrease
416 near the cloud top due to evaporation and entrainment (Suzuki et al., 2010). The uncertainties from assumed
417 hydrometeor size distributions and CFODD construction should be carefully considered when using the CFODD to
418 evaluate model droplet collection efficiencies against observations and in the application as an ERFaci constraint.
419 Simulated reflectivity biases affect the evaluation of the model CFODD slope against the observational CFODD slope
420 and thus affect the estimation of ERFaci bias.

421 A few additional limitations on CFODD analysis are imposed by biases in E3SMv2 SLWC representation. The ERFaci
422 constraint is restricted to the small and medium R_e CFODDs because of the underrepresentation of SLWCs with large
423 R_e . SLWCs with medium R_e are also underrepresented in E3SMv2, further limiting the CFODD analysis of E3SMv2
424 ERFaci because process perturbations are limited to the extent that they do not significantly reduce the number of
425 SLWCs with medium R_e . The high reflectivity near cloud top at $ICOD < 4$ in E3SMv2 CFODDs presents another
426 limitation. SLWCs with $COT < 4$ represent a significant fraction of the SLWC population in both A-Train and
427 E3SMv2 (Fig. 2), so including optically thin SLWCs in the linear regression would likely affect the CFODD slope
428 and droplet collection efficiency estimates.

429 Despite these limitations and the uncertainty associated with estimates of droplet collection efficiency from simulated
430 radar reflectivity, CFODD analysis offers a highly desired process-oriented constraint on ERFaci due to warm rain
431 processes. In E3SMv2, the CFODD slope exhibits the expected behavior in response to autoconversion perturbations:
432 slope increases with perturbations that increase the autoconversion rate and decreases with perturbations that decrease
433 the autoconversion rate. Our results also show that the model $ERFaci_{sw}$ is highly sensitive to the processes that the
434 CFODD represents, enabling the constraint of $ERFaci_{sw}$ against the CFODD slope derived from MODIS-CloudSat
435 cloud retrievals. Prior studies have demonstrated that radar reflectivity biases can be partially mitigated by bringing
436 the forward simulator into better agreement with the host model's microphysics parameterization and subgrid
437 variability (Song et al., 2018b; J. Wang et al., 2021). Modified versions of COSP featuring improved consistency with



438 E3SM are to be implemented in future E3SM model versions, which will decrease the uncertainties associated with
439 CFODD analysis of E3SM.

440 **6 Summary**

441 In this study, we present an updated CFODD analysis and demonstrate how it can be applied to ESMs as a process-
442 oriented constraint on ERFaci. When E3SMv2's droplet collection efficiency is constrained by MODIS-CloudSat
443 retrievals, E3SMv2's ERFaci_{sw} is reduced by 13%. Demonstrated here as a constraint based on autoconversion,
444 CFODD analysis represents a highly desirable constraint on a process, circumventing the equifinality issue that
445 bedevils atmospheric state variable-based approaches (Mülmenstädt et al., 2020). While this study focuses on
446 autoconversion, CFODD analysis could potentially apply to any microphysical process parameterization that affects
447 droplet collection efficiency (e.g., accretion, drop breakup, evaporation) to generate additional ERFaci constraints.

448 Several updates to the WRDs package in COSPv2.0 were made to support the application of CFODD analysis to
449 ESMs. In addition to the original WRDs diagnostics featuring relative frequencies of SLWCs by precipitation intensity
450 and the CFODD by R_e , we have implemented additional diagnostics in the WRDs that include all-sky SLWC
451 frequency maps and MODIS SLWC COT distributions for CFODD sampling statistics. Other updates include the
452 estimation of CFODD slopes using Random Sample Consensus robust linear regression and changes to the SLWC
453 detection schemes for better comparison between observations and satellite simulators.

454 In addition to the modifications of the WRDs described above, the MODIS and CloudSat observational reference data
455 has been updated for consistency with COSPv2.0 SLWC detection. SLWC detection is increased 5-fold in the updated
456 reference data. The increase in SLWC sampling also significantly affected the CFODD distributions and consequently,
457 the A-Train reference droplet collection efficiency at large R_e ($18 \mu\text{m} \leq R_e < 30 \mu\text{m}$). The updated WRDs showed that
458 droplet collection efficiencies in E3SMv2 are decreased compared to observations and SLWCs with small MODIS R_e
459 ($5 \mu\text{m} \geq R_e > 12 \mu\text{m}$) are overrepresented. The E3SMv2 CFODD results also show that simulated reflectivity profiles
460 near the cloud top are decoupled from the cloud below. The updates described herein have increased the WRDs'
461 utility for evaluating model warm rain process representation and support the analysis needed to derive a constraint
462 on ERFaci from CFODD analysis. Through an evaluation of E3SMv2, we demonstrate that the updated WRDs
463 illuminate specific biases in SLWC representation and provide contextual sampling statistics that are critical for
464 interpreting CFODD results and thus, for future applications of this observational constraint on ERFaci.



465

466 *Code and Data Availability:* The CloudSat and MODIS data products are available from the CloudSat Data Processing
467 Center at CIRA/Colorado State University (<https://www.cloudsat.cira.colostate.edu/>; last access: June 28, 2023). The
468 reference A-Train data used in this study is available here: <https://doi.org/10.5281/zenodo.8384180>. The modified
469 source code of COSPv2.0 is available here: <https://doi.org/10.5281/zenodo.8371120> and the E3SMv2 source code is
470 available here: <https://github.com/E3SM-Project/E3SM> (last access: September 27, 2023). The python package for
471 the two-dimensional Kolmogorov-Smirnov test applied in this study is available here
472 (<https://github.com/syrte/ndtest/tree/master>; last access: June 28, 2023). The python package scikit-learn was used for
473 robust linear regression analysis (<https://scikit-learn.org/stable/>; last access: June 28, 2023).

474 *Author contributions:* CMB led the project, developed the additional WRDs diagnostics in this study, performed the
475 model simulations and wrote the manuscript. PLM provided critical project guidance and support for modeling and
476 analysis. MWC led the A-Train observations analysis and provided guidance on additional WRDs diagnostics
477 development. AV provided input on CFODD analysis applications. JM provided guidance on ERFaci analysis. TM
478 and KS provided guidance on WRDs applications. All authors contributed to writing the manuscript.

479 *Competing Interests:* At least one of the (co-)authors is a member of the editorial board of Atmospheric Chemistry
480 and Physics.

481 *Acknowledgements:* The study was supported as part of the Enabling Aerosol–cloud interactions at GLObal
482 convection-permitting scales (EAGLES) project (project no. 74358) sponsored by the United States Department of
483 Energy (DOE), Office of Science, Office of Biological and Environmental Research (BER), Earth System Model
484 Development (ESMD) program area. The Pacific Northwest National Laboratory (PNNL) is operated for the DOE by
485 the Battelle Memorial Institute under Contract DE-AC05-76RL01830. The research used high-performance
486 computing resources from the PNNL Research Computing, the BER Earth System Modeling program's Compy
487 computing cluster located at PNNL, and resources of the National Energy Research Scientific Computing Center
488 (NERSC), a U.S. Department of Energy Office of Science User Facility located at Lawrence Berkeley National
489 Laboratory, operated under Contract No. DE-AC02-05CH11231, using NERSC awards ALCC-ERCAP0025938 and
490 BER-ERCAP0024471.



491 *Financial support.* This study was funded by the U.S. Department of Energy, Office of Science, Office of Biological
492 and Environmental research, Earth System Model Development (ESMD) program area (project nos. 74358). KS and
493 TM were supported by the Japan Society for the Promotion of Science KAKENHI (Grant JP19H05669), MEXT
494 program for the Advanced Studies of Climate Change Projection (SENTAN) (Grant JPMXD0722680395), and the
495 Environment Research and Technology Development Fund (S-20) (Grant JPMEERF21S12004) of the Environmental
496 Restoration and Conservation Agency. TM was supported by the JST FOREST Program (Grant JPMJFR206Y),
497 and the Japan Society for the Promotion of Science KAKENHI (Grant JP 23K13171).

498

499

500 **References**

- 501 Bellouin, N., Quaas, J., Gryspeerdt, E., Kinne, S., Stier, P., Watson-Parris, D., Boucher, O., Carslaw, K. S.,
502 Christensen, M., Daniau, A.-L., Dufresne, J.-L., Feingold, G., Fiedler, S., Forster, P., Gettelman, A.,
503 Haywood, J. M., Lohmann, U., Malavelle, F., Mauritsen, T., ... Stevens, B. (2020). Bounding Global Aerosol
504 Radiative Forcing of Climate Change. *Reviews of Geophysics*, *58*(1), e2019RG000660.
505 <https://doi.org/https://doi.org/10.1029/2019RG000660>
- 506 Bogenschutz, P. A., Gettelman, A., Morrison, H., Larson, V. E., Craig, C., & Schanen, D. P. (2013). Higher-Order
507 Turbulence Closure and Its Impact on Climate Simulations in the Community Atmosphere Model. *Journal of*
508 *Climate*, *26*(23), 9655–9676. <https://doi.org/https://doi.org/10.1175/JCLI-D-13-00075.1>
- 509 Cesana, G., & Chepfer, H. (2012). How well do climate models simulate cloud vertical structure? A comparison
510 between CALIPSO-GOCCP satellite observations and CMIP5 models. *Geophysical Research Letters*, *39*(20).
511 <https://doi.org/https://doi.org/10.1029/2012GL053153>
- 512 Christensen, M. W., Stephens, G. L., & Lebsack, M. D. (2013). Exposing biases in retrieved low cloud properties
513 from CloudSat: A guide for evaluating observations and climate data. *Journal of Geophysical Research:*
514 *Atmospheres*, *118*(21), 12, 112–120, 131. <https://doi.org/https://doi.org/10.1002/2013JD020224>
- 515 Gelaro, R., McCarty, W., Suárez, M. J., Todling, R., Molod, A., Takacs, L., Randles, C. A., Darmenov, A.,
516 Bosilovich, M. G., Reichle, R., Wargan, K., Coy, L., Cullather, R., Draper, C., Akella, S., Buchard, V.,
517 Conaty, A., da Silva, A. M., Gu, W., ... Zhao, B. (2017). The Modern-Era Retrospective Analysis for
518 Research and Applications, Version 2 (MERRA-2). *Journal of Climate*, *30*(14), 5419–5454.
519 <https://doi.org/10.1175/JCLI-D-16-0758.1>
- 520 Ghan, S. J. (2013). Technical Note: Estimating aerosol effects on cloud radiative forcing. *Atmospheric Chemistry*
521 *and Physics*, *13*(19), 9971–9974. <https://doi.org/10.5194/acp-13-9971-2013>
- 522 Golaz, J. C., Larson, V. E., & Cotton, W. R. (2002). A PDF-based model for boundary layer clouds. Part I: Method
523 and model description. *Journal of the Atmospheric Sciences*, *59*(24), 3540–3551.
524 [https://doi.org/10.1175/1520-0469\(2002\)059<3540:APBMFB>2.0.CO;2](https://doi.org/10.1175/1520-0469(2002)059<3540:APBMFB>2.0.CO;2)
- 525 Golaz, J.-C., Van Roekel, L. P., Zheng, X., Roberts, A. F., Wolfe, J. D., Lin, W., Bradley, A. M., Tang, Q., Maltrud,
526 M. E., Forsyth, R. M., Zhang, C., Zhou, T., Zhang, K., Zender, C. S., Wu, M., Wang, H., Turner, A. K., Singh,
527 B., Richter, J. H., ... Bader, D. C. (2022). The DOE E3SM Model Version 2: Overview of the Physical Model
528 and Initial Model Evaluation. *Journal of Advances in Modeling Earth Systems*, *14*(12), e2022MS003156.
529 <https://doi.org/https://doi.org/10.1029/2022MS003156>



- 530 Jing, X., Suzuki, K., & Michibata, T. (2019). The Key Role of Warm Rain Parameterization in Determining the
531 Aerosol Indirect Effect in a Global Climate Model. *Journal of Climate*, 32(14), 4409–4430.
532 <https://doi.org/https://doi.org/10.1175/JCLI-D-18-0789.1>
- 533 Kay, J. E., Wall, C., Yettella, V., Medeiros, B., Hannay, C., Caldwell, P., & Bitz, C. (2016). Global climate impacts
534 of fixing the Southern Ocean shortwave radiation bias in the Community Earth System Model (CESM).
535 *Journal of Climate*, 29(12), 4617–4636. <https://doi.org/10.1175/JCLI-D-15-0358.1>
- 536 Khairoutdinov, M., & Kogan, Y. (2000). A New Cloud Physics Parameterization in a Large-Eddy Simulation Model
537 of Marine Stratocumulus. *Monthly Weather Review*, 128(1), 229–243.
538 [https://doi.org/https://doi.org/10.1175/1520-0493\(2000\)128<0229:ANCPPI>2.0.CO;2](https://doi.org/https://doi.org/10.1175/1520-0493(2000)128<0229:ANCPPI>2.0.CO;2)
- 539 Larson, V. E. (2017). *CLUBB-SILHS: A parameterization of subgrid variability in the atmosphere*.
540 <http://arxiv.org/abs/1711.03675>
- 541 Larson, V. E., & Golaz, J.-C. (2005). Using Probability Density Functions to Derive Consistent Closure
542 Relationships among Higher-Order Moments. *Monthly Weather Review*, 133(4), 1023–1042.
543 <https://doi.org/https://doi.org/10.1175/MWR2902.1>
- 544 Liu, X., Easter, R. C., Ghan, S. J., Zaveri, R., Rasch, P., Shi, X., Lamarque, J. F., Gettelman, A., Morrison, H., Vitt,
545 F., Conley, A., Park, S., Neale, R., Hannay, C., Ekman, A. M. L., Hess, P., Mahowald, N., Collins, W.,
546 Iacono, M. J., ... Mitchell, D. (2012). Toward a minimal representation of aerosols in climate models:
547 Description and evaluation in the Community Atmosphere Model CAM5. *Geoscientific Model Development*,
548 5(3), 709–739. <https://doi.org/10.5194/GMD-5-709-2012>
- 549 Liu, X., Ma, P.-L., Wang, H., Tilmes, S., Singh, B., Easter, R. C., Ghan, S. J., & Rasch, P. J. (2016). Description and
550 evaluation of a new four-mode version of the Modal Aerosol Module (MAM4) within version 5.3 of the
551 Community Atmosphere Model. *Geoscientific Model Development*, 9(2), 505–522.
552 <https://doi.org/10.5194/gmd-9-505-2016>
- 553 Mangla, R., Indu, J., & Lakshmi, V. (2020). Evaluation of convective storms using spaceborne radars over the Indo-
554 Gangetic Plains and western coast of India. *Meteorological Applications*, 27(3), e1917.
555 <https://doi.org/https://doi.org/10.1002/met.1917>
- 556 Marchand, R., Mace, G. G., Ackerman, T., & Stephens, G. (2008). Hydrometeor Detection Using Cloudsat—An
557 Earth-Orbiting 94-GHz Cloud Radar. *Journal of Atmospheric and Oceanic Technology*, 25(4), 519–533.
558 <https://doi.org/10.1175/2007JTECHA1006.1>
- 559 Michibata, T., Kawamoto, K., & Takemura, T. (2014). The effects of aerosols on water cloud microphysics
560 and macrophysics based on satellite-retrieved data over East Asia and the North Pacific. *Atmospheric
561 Chemistry and Physics*, 14(21), 11935–11948. <https://doi.org/10.5194/acp-14-11935-2014>
- 562 Michibata, T., Suzuki, K., Ogura, T., & Jing, X. (2019a). *Data for the publication “Incorporation of inline warm
563 rain diagnostics into the COSP2 satellite simulator for process-oriented model evaluation.” Zenodo.*
564 <https://doi.org/10.5281/zenodo.3370823>
- 565 Michibata, T., Suzuki, K., Ogura, T., & Jing, X. (2019b). Incorporation of inline warm rain diagnostics into the
566 COSP2 satellite simulator for process-oriented model evaluation. *Geoscientific Model Development*, 12(10),
567 4297–4307. <https://doi.org/10.5194/gmd-12-4297-2019>
- 568 Mühlmenstädt, J., Nam, C., Salzmann, M., Kretzschmar, J., L’Ecuyer, T. S., Lohmann, U., Ma, P.-L., Myhre, G.,
569 Neubauer, D., Stier, P., Suzuki, K., Wang, M., & Quaas, J. (2020). Reducing the aerosol forcing uncertainty
570 using observational constraints on warm rain processes. *Science Advances*, 6(22), eaaz6433.
571 <https://doi.org/10.1126/sciadv.aaz6433>



- 572 Platnick, S., Meyer, K. G., King, M. D., Wind, G., Amarasinghe, N., Marchant, B., Arnold, G. T., Zhang, Z.,
573 Hubanks, P. A., Holz, R. E., Yang, P., Ridgway, W. L., & Riedi, J. (2017). The MODIS Cloud Optical and
574 Microphysical Products: Collection 6 Updates and Examples From Terra and Aqua. *IEEE Transactions on*
575 *Geoscience and Remote Sensing*, 55(1), 502–525. <https://doi.org/10.1109/TGRS.2016.2610522>
- 576 Rasch, P. J., Xie, S., Ma, P. L., Lin, W., Wang, H., Tang, Q., Burrows, S. M., Caldwell, P., Zhang, K., Easter, R. C.,
577 Cameron-Smith, P., Singh, B., Wan, H., Golaz, J. C., Harrop, B. E., Roesler, E., Bacmeister, J., Larson, V. E.,
578 Evans, K. J., ... Yang, Y. (2019). An Overview of the Atmospheric Component of the Energy Exascale Earth
579 System Model. *Journal of Advances in Modeling Earth Systems*, 11(8), 2377–2411.
580 <https://doi.org/10.1029/2019MS001629>
- 581 Song, H., Zhang, Z., Ma, P.-L., Ghan, S. J., & Wang, M. (2018a). An Evaluation of Marine Boundary Layer Cloud
582 Property Simulations in the Community Atmosphere Model Using Satellite Observations: Conventional
583 Subgrid Parameterization versus CLUBB. *Journal of Climate*, 31(6), 2299–2320.
584 <https://doi.org/https://doi.org/10.1175/JCLI-D-17-0277.1>
- 585 Song, H., Zhang, Z., Ma, P.-L., Ghan, S., & Wang, M. (2018b). The importance of considering sub-grid cloud
586 variability when using satellite observations to evaluate the cloud and precipitation simulations in climate
587 models. *Geoscientific Model Development*, 11(8), 3147–3158. <https://doi.org/10.5194/gmd-11-3147-2018>
- 588 Stephens, G. L., L'Ecuyer, T., Forbes, R., Gettelmen, A., Golaz, J.-C., Bodas-Salcedo, A., Suzuki, K., Gabriel, P., &
589 Haynes, J. (2010). Dreary state of precipitation in global models. *Journal of Geophysical Research: Atmospheres*, 115(D24). <https://doi.org/https://doi.org/10.1029/2010JD014532>
- 591 Suzuki, K., Nakajima, T. Y., & Stephens, G. L. (2010). Particle Growth and Drop Collection Efficiency of Warm
592 Clouds as Inferred from Joint CloudSat and MODIS Observations. *Journal of the Atmospheric Sciences*,
593 67(9), 3019–3032. <https://doi.org/10.1175/2010JAS3463.1>
- 594 Suzuki, K., Stephens, G., Bodas-Salcedo, A., Wang, M., Golaz, J.-C., Yokohata, T., & Koshiro, T. (2015).
595 Evaluation of the Warm Rain Formation Process in Global Models with Satellite Observations. *Journal of the*
596 *Atmospheric Sciences*, 72(10), 3996–4014. <https://doi.org/https://doi.org/10.1175/JAS-D-14-0265.1>
- 597 Suzuki, K., Stephens, G. L., & Lebsock, M. D. (2013). Aerosol effect on the warm rain formation process: Satellite
598 observations and modeling. *Journal of Geophysical Research: Atmospheres*, 118(1), 170–184.
599 <https://doi.org/https://doi.org/10.1002/jgrd.50043>
- 600 Wang, H., Easter, R. C., Zhang, R., Ma, P. L., Singh, B., Zhang, K., Ganguly, D., Rasch, P. J., Burrows, S. M.,
601 Ghan, S. J., Lou, S., Qian, Y., Yang, Y., Feng, Y., Flanner, M., Leung, R. L., Liu, X., Shrivastava, M., Sun, J.,
602 ... Yoon, J. H. (2020). Aerosols in the E3SM Version 1: New Developments and Their Impacts on Radiative
603 Forcing. *Journal of Advances in Modeling Earth Systems*, 12(1). <https://doi.org/10.1029/2019MS001851>
- 604 Wang, J., Fan, J., Houze, R. A., Brodzik, S. R., Zhang, K., Zhang, G. J., & Ma, P. L. (2021). Using radar
605 observations to evaluate 3-D radar echo structure simulated by the Energy Exascale Earth System Model
606 (E3SM) version 1. *Geoscientific Model Development*, 14(2), 719–734. <https://doi.org/10.5194/gmd-14-719-2021>
- 608 Wood, R. (2005). Drizzle in Stratiform Boundary Layer Clouds. Part II: Microphysical Aspects. *Journal of the*
609 *Atmospheric Sciences*, 62(9), 3034–3050. <https://doi.org/https://doi.org/10.1175/JAS3530.1>
- 610 Zhang, G. J., & McFarlane, N. A. (1995). Sensitivity of climate simulations to the parameterization of cumulus
611 convection in the Canadian climate centre general circulation model. *Atmosphere-Ocean*, 33(3), 407–446.
612 <https://doi.org/10.1080/07055900.1995.9649539>
- 613 Zhang, M., Xie, S., Liu, X., Lin, W., Zhang, K., Ma, H.-Y., Zheng, X., & Zhang, Y. (2020). Toward Understanding
614 the Simulated Phase Partitioning of Arctic Single-Layer Mixed-Phase Clouds in E3SM. *Earth and Space*
615 *Science*, 7(7), e2020EA001125. <https://doi.org/https://doi.org/10.1029/2020EA001125>



- 616 Zhang, M., Xie, S., Liu, X., Lin, W., Zheng, X., Golaz, J.-C., & Zhang, Y. (2022). Cloud Phase Simulation at High
617 Latitudes in EAMv2: Evaluation Using CALIPSO Observations and Comparison With EAMv1. *Journal of*
618 *Geophysical Research: Atmospheres*, 127(22), e2022JD037100.
619 <https://doi.org/https://doi.org/10.1029/2022JD037100>
- 620 Zhang, Y., Klein, S. A., Boyle, J., & Mace, G. G. (2010). Evaluation of tropical cloud and precipitation statistics of
621 Community Atmosphere Model version 3 using CloudSat and CALIPSO data. *Journal of Geophysical*
622 *Research: Atmospheres*, 115(D12). <https://doi.org/https://doi.org/10.1029/2009JD012006>
- 623 Zhang, Y., Xie, S., Lin, W., Klein, S. A., Zelinka, M., Ma, P.-L., Rasch, P. J., Qian, Y., Tang, Q., & Ma, H.-Y.
624 (2019a). Evaluation of Clouds in Version 1 of the E3SM Atmosphere Model With Satellite Simulators.
625 *Journal of Advances in Modeling Earth Systems*, 11(5), 1253–1268.
626 <https://doi.org/https://doi.org/10.1029/2018MS001562>
- 627 Zhang, Y., Xie, S., Lin, W., Klein, S. A., Zelinka, M., Ma, P.-L., Rasch, P. J., Qian, Y., Tang, Q., & Ma, H.-Y.
628 (2019b). Evaluation of Clouds in Version 1 of the E3SM Atmosphere Model With Satellite Simulators.
629 *Journal of Advances in Modeling Earth Systems*, 11(5), 1253–1268.
630 <https://doi.org/https://doi.org/10.1029/2018MS001562>
- 631
- 632
- 633